

TSD-SR: One-Step Diffusion with Target Score Distillation for Real-World Image Super-Resolution

Linwei Dong^{1,2*} Qingnan Fan^{2*} Yihong Guo¹ Zhonghao Wang³
 Qi Zhang² Jinwei Chen² Yawei Luo^{1†} Changqing Zou^{1,4}

¹Zhejiang University ²Vivo Mobile Communication Co. Ltd
³University of Chinese Academy of Sciences ⁴Zhejiang Lab

Abstract

Pre-trained text-to-image diffusion models are increasingly applied to real-world image super-resolution (Real-ISR) tasks. Given the iterative refinement nature of diffusion models, most existing approaches are computationally expensive. While methods such as SinSR and OSEDiff have emerged to condense inference steps via distillation, their performance in image restoration or details recovery is not satisfactory. To address this, we propose TSD-SR, a novel distillation framework specifically designed for real-world image super-resolution, aiming to construct an efficient and effective one-step model. We first introduce the Target Score Distillation, which leverages the priors of diffusion models and real image references to achieve more realistic image restoration. Secondly, we propose a Distribution-Aware Sampling Module to make detail-oriented gradients more readily accessible, addressing the challenge of recovering fine details. Extensive experiments demonstrate that our TSD-SR has superior restoration results (most of the metrics perform the best) and the fastest inference speed (e.g. 40 times faster than SeeSR) compared to the past Real-ISR approaches based on pre-trained diffusion priors. Our code is released at <https://github.com/Microtreei/TSD-SR>.

1. Introduction

Image super-resolution (ISR) [8, 9, 23, 26] aims to transform low-quality (LQ) images, which have been degraded by noise or blur, into clear high-quality (HQ) images. Unlike traditional ISR methods [6, 67], which assume a known degradation process, real-world image super-resolution (Real-ISR) [47, 63] focuses on enhancing images affected by complex and unknown degradations, thereby offering greater practical utility.

*Equal contribution. †Corresponding authors.

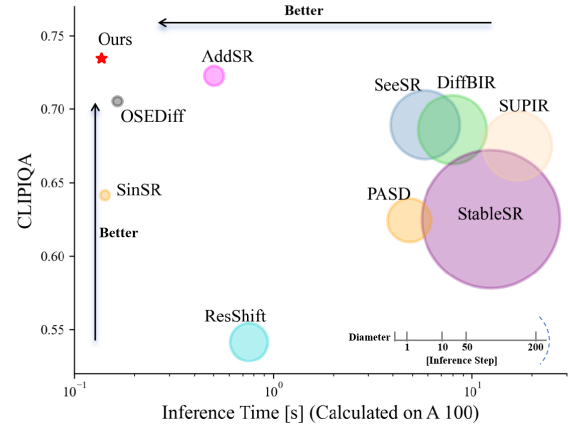


Figure 1. Performance and efficiency comparison among Real-ISR methods. TSD-SR stands out for achieving high-quality restoration with the fastest speed among diffusion-based models. In contrast, existing models prioritize either speed or restoration performance. The performance of each method is benchmarked on an A100 GPU with the DRealSR dataset.

Generative models, particularly Generative Adversarial Networks (GANs) [11, 33, 37] and Diffusion Models (DMs) [17, 40, 42], have demonstrated remarkable capabilities in tackling Real-ISR tasks. GAN-based methods utilize adversarial training by alternately optimizing a generator and a discriminator to produce realistic images. While GANs support one-step inference, they are often hindered by challenges such as mode collapse and training instability [2]. Recently, Diffusion Models (DMs) have demonstrated impressive performance in image generation [21, 48]. Their strong priors enable them to produce more realistic images with richer details compared to GAN-based methods [40, 42]. Some researchers [29, 54, 57, 61] have successfully leveraged pre-trained DMs for Real-ISR tasks. However, due to the iterative denoising nature of diffusion models [17], the Real-ISR process is computationally expensive.

To achieve an efficient and one-step network akin to GANs, several pioneering methods that condense the iterations of diffusion models through distillation [12, 15, 18, 58] have been proposed [49, 53, 55]. Among these works, OSEDiff [53] introduced the Variational Score Distillation (VSD) loss [51] to Real-ISR tasks, achieving state-of-the-art (SOTA) one-step performance by leveraging prior knowledge from pre-trained models. Despite these advancements, our investigation has revealed two critical limitations associated with VSD in Real-ISR applications. **(1) Unreliable gradient direction.** VSD relies on a Teacher Model to provide a “true gradient direction.” However, this guidance is proven unreliable in scenarios where initial ISR outputs are suboptimal. **(2) Insufficient detail recovery.** The VSD loss exhibits notable variation across different timesteps, and the uniform sampling strategy for t poses challenges in aligning the score function with detailed texture recovery requirements. These findings underscore the need for more effective approaches to address these issues.

In this paper, we propose a novel method called **TSD-SR** to distill a multi-step Text-to-Image (T2I) DMs [10, 38, 40] into an effective one-step diffusion model tailored for the Real-ISR task. Specifically, TSD-SR consists of two components: **Target Score Distillation (TSD)** and **Distribution-Aware Sampling Module (DASM)**. TSD incorporates our newly proposed Target Score Matching (TSM) loss to compensate for the limitations of the VSD loss. This significant score loss leverages HQ data to provide a reliable optimization trajectory during distillation, effectively reducing visual artifacts caused by deviant predictions from the Teacher Model. DASM is designed to enhance detail recovery by strategically sampling low-noise samples that are distribution-based during training. This approach effectively allocates more optimization to early timesteps within a single iteration, thereby improving the recovery of fine details.

Experiments on popular benchmarks demonstrate that TSD-SR achieves superior restoration performance (most of the metrics perform the best) and high efficiency (the fastest inference speed, 40 times faster than SeeSR) compared to the state-of-the-art Real-ISR methods based on pre-trained DMs, while requiring only a single inference step, as shown in (Fig. 1).

Our main contribution can be summarized as threefold:

- We propose a novel method called TSD-SR to achieve one-step DMs distillation for the Real-ISR task.
- We introduce Target Score Distillation (TSD) to provide reliable gradients that enhance the realism of outputs from Real-ISR methods.
- We design a Distribution-Aware Sampling Module (DASM) specifically tailored to enhance the capability of detail restoration.

2. Related Work

GAN-based Real-ISR. Since SRGAN [26] first applied GAN to ISR, it has effectively enhanced visual quality by combining adversarial loss with perceptual loss [7, 66]. Subsequently, ESRGAN [46] introduced Residual-in-Residual Dense Block and a relativistic average discriminator, further improving detail restoration. Methods like BSRGAN [63] and Real-ESRGAN [47] simulate complex real-world degradation processes, achieving ISR under unknown degradation conditions, which enhances the model’s generalization ability. Although GAN-based methods are capable of adding more realistic details to images, they suffer from training instability and mode collapse [2].

Multi-step Diffusion-based Real-ISR. Some researches [29, 45, 54, 57, 61] in recent years have utilized the powerful image priors in pre-trained T2I diffusion models [35, 40, 65] for Real-SR tasks and achieved promising results. For example, StableSR [45] balances fidelity and perceptual quality by fine-tuning the time-aware encoder and employing controllable feature wrapping. DiffBiR [29] first processes the LR image through a reconstruction network and then uses the Stable Diffusion (SD) model [40] to supplement the details. SeeSR [54] attempts to better stimulate the generative power of the SD model by extracting the semantic information in the image as a conditional guide. PASD [57] introduces a pixel-aware cross attention module to enable the diffusion model to perceive the local structure of the image at the pixel level, while using a degradation removal module to extract degradation insensitive features to guide the diffusion process along with high-level information from the image. SUPIR [61] achieves a generative and fidelity capability using negative cues [16] as well as restoration-guided sampling, while using a larger pre-training model with a larger dataset to enhance the model capability. However, all of these methods are limited by the multi-step denoising of the diffusion model, which requires 20-50 iterations in inference, resulting in an inference time that lags far behind that of GAN-based methods.

One-step Diffusion-based Real-ISR. Recently, there has been a surge of interest within the academic community in one-step distillation techniques [31, 34, 41, 59, 60] for diffusion-based Real-ISR task. SinSR [49] leverages consistency preserving distillation to condense the inference steps of ResShift [62] into a single step, yet the generalization of ResShift and SinSR is constrained due to the absence of large-scale data training. AddSR [55] introduces the adversarial diffusion distillation (ADD) [41] to Real-ISR tasks, resulting in a comparatively effective four-step model. However, this method has a propensity to produce excessive and unnatural image details. OSEDiff [53] directly uses LQ images as the beginning of the diffusion process, and employs VSD loss [51] as a regularization technique to condense a multi-step pre-trained T2I model into a

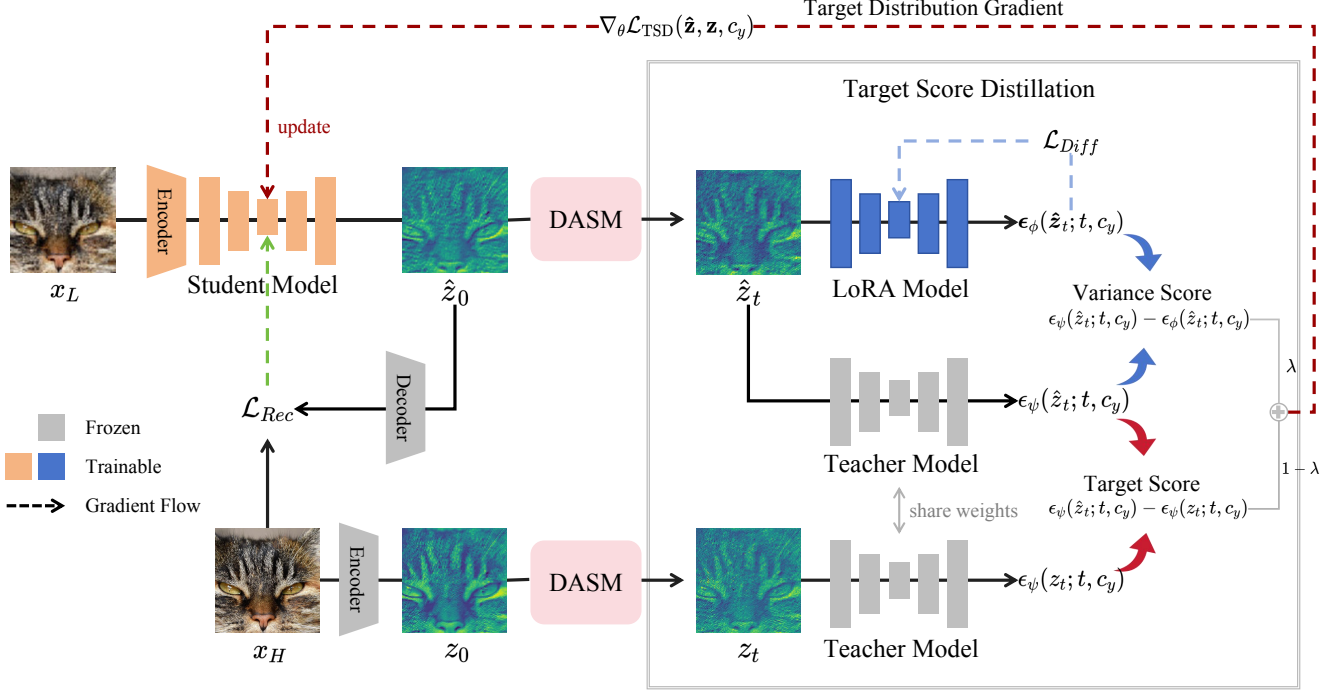


Figure 2. Pipeline overview. We train a one-step Student Model G_θ to transform the low-quality image x_L into a more realistic one. The noisy latent \hat{z}_t sampled by DASM (Details can be found in Fig. 6.) will be fed into both the pre-trained Teacher and the LoRA Model to produce the Variational Score Loss. Subsequently, the Teacher’s predictions on \hat{z}_t and z_t yield the Target Score Loss. Their weighted forms, namely TSD (red flow), along with the pixel-space reconstruction loss (green flow), are leveraged to update the Student Model G_θ . After updating the Student Model, we employ the diffusion loss (blue flow) to update the LoRA Model.

one-step Real-ISR model. However, due to the incorporation of alternating training strategies, OSediff may initially tend towards unreliable optimization directions, which may lead to visual artifacts.

3. Methodology

3.1. Preliminaries

Problem Formulation. The ISR problem aims to reconstruct a HQ image x_H from an LQ input x_L by training a parameterized ISR model G_θ on a dataset $\mathcal{D} = \{(x_L, x_H)_{i=1}^N\}$, where N represents the number of image pairs. Formally, this problem can be formulated as minimizing the following objective:

$$\theta^* = \arg \min_{\theta} \mathbb{E}_{(x_L, x_H) \sim \mathcal{D}} [\mathcal{L}_{Rec}(G_\theta(x_L), x_H) + \lambda \mathcal{L}_{Reg}(q_\theta(\hat{x}_H), p(x_H))] \quad (1)$$

Here, \mathcal{L}_{Rec} denotes the reconstruction loss, commonly measured by distance metrics such as L_2 or $LPIPS$ [66]. The regularization term \mathcal{L}_{Reg} improves the realism and generalization of the output of the ISR model. This objective can be understood as aligning the ISR output \hat{x}_H ’s distribution, $q_\theta(\hat{x}_H)$, with the high-quality data x_H ’s distribution $p(x_H)$

by minimizing the KL-divergence [25]:

$$\min_{\theta} \mathcal{D}_{KL}(q_\theta(\hat{x}_H) || p(x_H)) \quad (2)$$

While several studies [46, 47, 63] have employed adversarial loss to optimize this objective, they often encounter issues like mode collapse and training instability. Recent work [53] achieved state-of-the-art results using Variational Score Distillation (VSD) as the regularization loss to minimize this objective, which inspires our research.

Variational Score Distillation. Variational Score Distillation (VSD) [51] was initially introduced for text-to-3D generation, by distilling a pre-trained text-to-image diffusion model to optimize a single 3D representation [36].

In the VSD framework, a pre-trained diffusion model, represented as ϵ_ψ , and its trainable (LoRA [19]) replica ϵ_ϕ , are used to regularize the generator network G_θ . As outlined in ProlificDreamer [51], the gradient with respect to the generator parameters θ is formulated as follows:

$$\nabla_{\theta} \mathcal{L}_{VSD}(\hat{z}, c_y) = \mathbb{E}_{t, \epsilon} \left[\omega(t) (\epsilon_\psi(\hat{z}_t; t, c_y) - \epsilon_\phi(\hat{z}_t; t, c_y)) \frac{\partial \hat{z}}{\partial \theta} \right] \quad (3)$$

where $\hat{z}_t = \alpha_t \hat{z} + \sigma_t \epsilon$ is the noisy input, \hat{z} is the latent outputted by the generator network G_θ , ϵ is a Gaussian noise,

and α_t, σ_t are the noise-data scaling constants. c_y is a text embedding corresponding to a caption that describes the input image, and $w(t)$ is a time-varying weighting function.

3.2. Overview of TSD-SR

As depicted in Fig. 2, our goal is to distill a given pre-trained T2I DM into a fast one-step Student Model G_θ , using the Teacher Model ϵ_ψ and the trainable LoRA Model ϵ_ϕ . We denote the latent output of the distilled model as \hat{z}_0 , and the HQ latent representation as z_0 . Both \hat{z}_0 and z_0 are passed through our Distribution-Aware Sampling Module (DASM) to obtain distribution-based samples \hat{z}_t and z_t (Sec. 3.4). We train G_θ by minimizing the two losses: a reconstruction loss in pixel space to compare the model outputs against the ground truth, and a regularization loss (from Target Score Distillation) to enhance the realism (Sec. 3.3). After updating the Student Model, we update the LoRA Model with the diffusion loss. Finally, in Sec. 3.5, we present an overview of all the losses encountered during the training phase.

3.3. Target Score Distillation

Similar to [53], we introduce VSD loss into our work as a regularization term to enhance the realism and generalization of the G_θ 's outputs. Upon reviewing VSD Eq. (3), $\epsilon_\phi(\hat{z}_t; t, c_y)$ represents the current estimated gradient direction for G_θ 's noisy outputs \hat{z}_t , whereas $\epsilon_\psi(\hat{z}_t; t, c_y)$ corresponds to the ideal gradient direction guiding towards more realistic outputs. The overarching goal of model optimization is to align the suboptimal gradient direction with the superior direction based on pre-trained priors, thus facilitating the optimization of the Student distribution toward that of the Teacher. However, this strategy encounters hurdles, especially in the early training phase: the quality of synthetic latent \hat{z}_t is not high enough for the Teacher Model to provide a precise prediction. As illustrated in Fig. 3, the Teacher Model struggles to accurately predict the optimization direction for low-quality synthetic latent \hat{z}_t in the early stage, as indicated by a cosine similarity of only 0.2 to the ideal direction, compared to 0.88 for high-quality latent z_t . This problem can lead to severe visual artifacts, as is evident in Fig. 4(a).

A straightforward remedial measure is to employ a mean squared error (MSE) loss to align the synthetic latent with the ideal inputs of the Teacher Model, which are derived from the HQ latent. However, as shown in Fig. 4(b), this approach has been observed to lead to over-smoothed results [13]. Our strategy, instead, is to align the predictions made by the Teacher Model on both synthetic and HQ latent, thereby encouraging greater consistency between them. The core idea is that for samples drawn from the same distribution, the real scores predicted by the Teacher Model should be close to each other. We refer to this approach as

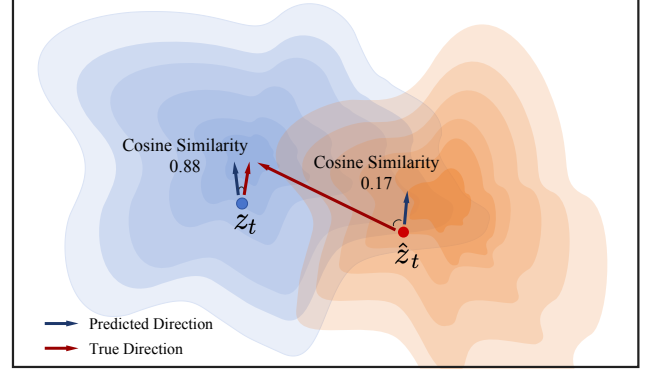


Figure 3. A visual comparison of the gradient direction. We set the timestep t to 100 and calculated the cosine similarity between the prediction directions from the Teacher Model and the true direction (towards the HQ data). The **prediction direction** for z_t closely matches the **true direction**, but not for \hat{z}_t , suggesting that suboptimal samples may lead to directional deviations.

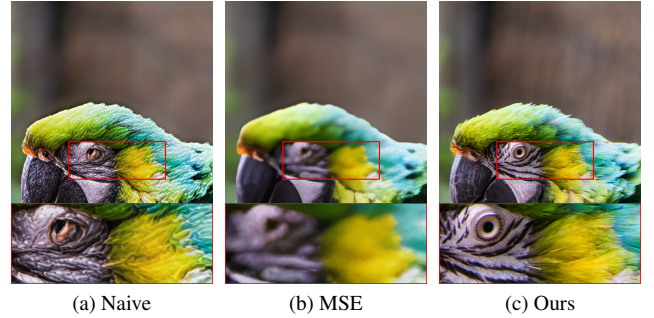


Figure 4. The visualization of different strategies. (a) The naive method introduces fake textures and fails to recover fine details. (b) MSE leads to over-smoothed generation results, lacking high-frequency information. (c) Our method offers the superior visual effects and fine textures.

Target Score Matching (TSM):

$$\begin{aligned} \nabla_{\theta} \mathcal{L}_{\text{TSM}}(\hat{z}, z, c_y) \\ = \mathbb{E}_{t, \epsilon} \left[w(t) (\epsilon_\psi(\hat{z}_t; t, c_y) - \epsilon_\psi(z_t; t, c_y)) \frac{\partial \hat{z}}{\partial \theta} \right] \end{aligned} \quad (4)$$

where the expectation of the gradient is computed across all diffusion timesteps $t \in \{1, \dots, T\}$ and $\epsilon \sim \mathcal{N}(0, I)$. Equation (4) encapsulates the optimization loss for our Target Score Matching. Upon examining it in conjunction with Eq. (3), we notice that VSD utilizes the prediction residual between the Teacher and the LoRA Model to drive gradient backpropagation. Similarly, our TSM employs the synthetic and the HQ data to produce the gradients. By blending these two strategies with hyperparameter weights λ and $1 - \lambda$, we construct a combined optimization loss that effectively unifies the strengths of both approaches, as formulated in

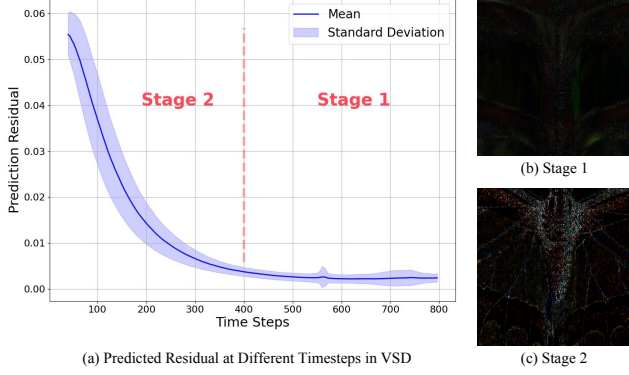


Figure 5. (a) The prediction errors of the VSD loss at different timesteps. The error divergence is more pronounced in early timesteps than later. This phenomenon is observed throughout the optimization process. (b) The visualization of Stage 1 prediction error. (c) The visualization of Stage 2 prediction error.

Eq. (5), to guide the training process.

$$\nabla_{\theta} \mathcal{L}_{\text{TSD}}(\hat{z}, z, c_y) = \mathbb{E}_{t, \epsilon} \left[w(t) [\epsilon_{\psi}(\hat{z}_t; t, c_y) - \epsilon_{\psi}(z_t; t, c_y) + \lambda (\epsilon_{\psi}(z_t; t, c_y) - \epsilon_{\phi}(\hat{z}_t; t, c_y))] \frac{\partial \hat{z}}{\partial \theta} \right] \quad (5)$$

where $w(t)$ is a time-aware weighting function tailored for Real-ISR. Other symbols are consistent with those previously defined. By introducing the prediction of the pre-trained diffusion model on HQ latent, we have circumvented the issue of the model falling into visual artifacts or producing over-smoothed results, as illustrated in Fig. 4(c).

3.4. Distribution-Aware Sampling Module

In the VSD-based framework, it is necessary to match the score functions predicted by the Teacher Model and the LoRA Model across timesteps $t \in 0, 1, \dots, T$. However, for the Real-ISR problem, this matching performance is inconsistent across timesteps, as illustrated in Fig. 5(a). This phenomenon may be attributed to the reliance on low-frequency (LF) priors in the LQ data, while lacking guidance from high-frequency (HF) details. The output sample \hat{z}_0 , derived from LQ data, contains low-frequency (LF) priors that are easily captured by the LoRA Model, resulting in similar predictions during LF restoration (Stage 1), as shown in Fig. 5(b). However, in Stage 2, due to the absence of high-frequency (HF) details in \hat{z}_0 , the LoRA Model struggles to reconstruct fine-grained features, leading to divergent predictions, as illustrated in Fig. 5(c). To address this issue, we aim to reduce such divergence.

Existing methods match the score function at each iteration using a single latent sample \hat{z}_t , with the timestep t drawn from a uniform distribution. This leads to slow convergence and even training difficulty during Stage 2, as gradients from important timesteps are diluted by uniform av-

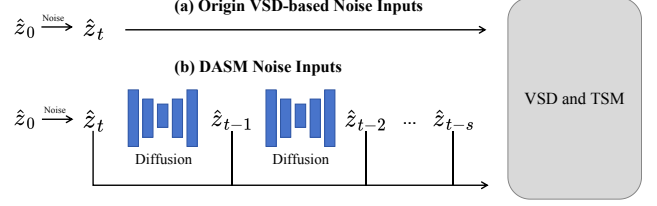


Figure 6. Illustration of DASM. Top: The naive approach that adds noise directly to the samples. Bottom: The proposed DASM leverages diffusion model priors to generate noisy latent that better align with the true sampling trajectory. These noisy samples can all serve as inputs to the downstream network, enabling effective gradient backpropagation.

eraging. To this end, we propose our Distribution-Aware Sampling Module (DASM). This module accumulates optimization gradients for earlier timestep samples in a single iteration, enabling the backpropagation of more gradients focused on detail optimization. As shown in Fig. 6, we first obtain the noisy synthetic latent representation as $\hat{z}_t = (1 - \sigma_t)\hat{z}_0 + \sigma_t\epsilon$, where σ_t is a weighting factor and ϵ denotes Gaussian noise. Subsequently, we employ a LoRA Model to perform denoising, yielding noisy samples at the previous timestep as described in Eq. (6):

$$\hat{z}_{t-1} = \hat{z}_t + (\sigma_{t-1} - \sigma_t) \cdot \epsilon_{\phi}(\hat{z}_t; t, c_y), \quad (6)$$

The parameters σ_{t-1} and σ_t are obtained from the flow matching scheduler. Here, the LoRA Model has learned the distribution of \hat{z}_0 . Similarly, z_{t-1} can be obtained by denoising using the Teacher Model. In a single iteration, gradients from noisy samples along the sampling trajectory can be accumulated to update the Student Model. Since these samples follow the diffusion sampling trajectory and are concentrated at early timesteps, this approach effectively reduces the divergence observed in Stage 2.

3.5. Training Objective

We summarize all the losses that we used in our framework. **Student Model G_{θ} .** We train our Student Model with the reconstruction loss \mathcal{L}_{Rec} and the regularization loss \mathcal{L}_{Reg} . For the reconstruction loss, we use the $LPIPS$ loss in the pixel space and the MSE loss in the latent space:

$$\begin{aligned} \mathcal{L}_{\text{Rec}}(G_{\theta}(x_L), x_H) \\ = \gamma_1 \mathcal{L}_{LPIPS}(G_{\theta}(x_L), x_H) + \mathcal{L}_{MSE}(z_t, \hat{z}_t). \end{aligned} \quad (7)$$

For the regularization loss, we use our TSD loss, Eq. (5). Therefore, the overall training objective for the Student Model G_{θ} is:

$$\mathcal{L}_{\text{Stu}} = \mathcal{L}_{\text{Rec}} + \gamma_2 \mathcal{L}_{\text{Reg}}, \quad (8)$$

where γ_1 and γ_2 are weighting factors. We initialize both γ_1 and γ_2 to 1 at the beginning of training. As optimization

progresses, we ramp up γ_1 from 1 to 2 while maintaining γ_2 at its initial value.

LoRA Model ϵ_ϕ . As stipulated by VSD, the replica ϵ_ϕ must be trainable, with its training objective being:

$$\mathcal{L}_{Diff}(\hat{z}, c_y) = \mathbb{E}_{t, \epsilon} [\|\epsilon_\phi(\hat{z}_t; t, c_y) - \epsilon'\|^2], \quad (9)$$

where ϵ' serves as the training target for the denoising network, representing Gaussian noise in the context of DDPM, and a gradient towards HQ data for flow matching.

4. Experiments

4.1. Experimental Settings

Training Datasets. For training, we utilize DIV2K [1], Flickr2K [43], LSDIR [27], and the first 10K face images from FFHQ [20]. To synthesize LR-HR pairs, we adopt the same degradation pipeline as in Real-ESRGAN [47].

Test Datasets. We evaluate our model on the synthetic DIV2K-Val [1] dataset, as well as two real-world datasets: RealSR [4] and DRealSR [52]. The real-world datasets consist of 128×128 low-quality (LQ) and 512×512 high-quality (HQ) image pairs. For the synthetic set, 3,000 pairs were generated by cropping 512×512 patches from DIV2K-Val and applying the Real-ESRGAN [47] degradation pipeline to downsample them to 128×128.

Evaluation Metrics. To evaluate our method, we employ both full-reference and no-reference metrics. The full-reference metrics include PSNR and SSIM [50] (computed on the Y channel of the YCbCr color space) for fidelity; LPIPS [66] and DISTS [7] for perceptual quality; and FID [14] for measuring distribution similarity. The no-reference metrics include NIQE [64], MANIQA [56], MUSIQ [22], and CLIPQA [44].

Compared Methods. We categorize the test models into two groups: single-step and multi-step inference. The single-step inference diffusion models include SinSR [49], AddSR [55], and OSediff [53]. The multi-step inference diffusion models comprise StableSR [45], ResShift [62], PASD [57], DiffBIR [29], SeeSR [54], SUPIR [61], and AddSR [55]. Specifically, for AddSR, we have conducted comparisons between its single-step and four-step models. GAN-based Real-ISR methods [5, 28, 47, 63] are detailed in the supplementary material.

Implementation Details. All models are initialized from the Teacher Model (SD3 [10] in our work). Similar to OSediff [53], we only train the VAE encoder and the denoising network in the Student Model, freezing the VAE decoder to preserve its prior [24]. We utilize the default prompt for the Student Model, while prompts are extracted from HQ images for the Teacher and LoRA models during training. We adopt the AdamW optimizer [30] with a learning rate of 5e-6 for the Student Model and 1e-6 for the LoRA Model, setting the LoRA rank to 64 for both models.

During the initial training phase, we incorporate MSE loss in the latent space and exclude DASM to stabilize training and reduce time cost. In later stages, we remove the MSE loss to avoid over-smoothed results and introduce DASM to enhance restoration quality. The training process took approximately 96 hours, utilizing 8 NVIDIA V100 GPUs with a batch size of 16.

4.2. Comparison with Existing Methods

Quantitative Comparisons. Tab. 1 shows the quantitative comparison of our method with other single-step diffusion models on three datasets. Our method achieves the best results across most evaluation metrics. SinSR and AddSR, as distilled versions of previous multi-step super-resolution methods, significantly reduce inference steps while suffering a corresponding drop in performance. OSediff introduces the VSD loss from 3D generation tasks into the Real-ISR without fully accounting for the substantial differences between the two domains. As a result, its no-reference image quality metrics are not satisfactory. In contrast, our proposed TSD-SR, specifically designed for Real-ISR, outperforms all other single-step models in the vast majority of key metrics.

Tab. 2 shows the quantitative comparison with multi-step models. We can draw the following conclusions: (1) TSD-SR demonstrates significant advantages over competing methods in terms of LPIPS, DISTS, and NIQE. Additionally, it outperforms most multi-step models in FID, MUSIQ, and CLIPQA. (2) DiffBIR, SeeSR, PASD, and AddSR achieve better results in terms of MANIQA, which may be attributed to the fact that multi-step models benefit from more denoising iterations to generate richer details. (3) ResShift stands out with the highest PSNR and SSIM scores, while StableSR also performs well in terms of DISTS and FID. However, both models underperform on the no-reference metrics.

Finally, we explain the relatively lower PSNR and SSIM scores observed in our experiments. Several studies [55, 61] have shown that these reconstruction metrics are not well-suited for the evaluation of Real-ISR tasks. Models that recover more realistic or detailed textures often yield lower PSNR and SSIM scores, reflecting a fundamental trade-off between perceptual quality and pixel-wise fidelity [3, 32, 68]. This phenomenon has also been extensively discussed in the other research work [3, 32, 45, 55, 61, 66, 68]. LPIPS [66] is proposed to overcome the limitation that PSNR and SSIM fail to align with human judgments in spatial ambiguities situations. Other DMs-based SR researchers [45, 61] argue that DMs introduce superior pre-trained priors, enabling the restoration of information that traditional methods (from scratch) cannot achieve. However, such capability often leads to a decline in pixel-level metrics, as they prioritize distribution modeling and sampling from learned

Table 1. Quantitative comparison with the state-of-the-art one-step methods across both synthetic and real-world benchmarks. The number of diffusion inference steps is indicated by ‘s’. The best results of each metric are highlighted in **red**.

Datasets	Method	PSNR \uparrow	SSIM \uparrow	LPIPS \downarrow	DISTS \downarrow	FID \downarrow	NIQE \downarrow	MUSIQ \uparrow	MANIQA \uparrow	CLIPQA \uparrow
DRealSR	OSDiff-1s	27.92	0.7836	0.2968	0.2162	135.51	6.4471	64.69	0.5898	0.6958
	AddSR-1s	27.77	0.7722	0.3196	0.2242	150.18	6.9321	60.85	0.5490	0.6188
	SinSR-1s	28.38	0.7497	0.3669	0.2484	172.72	6.9606	55.03	0.4904	0.6412
	Ours-1s	27.77	0.7559	0.2967	0.2136	134.98	5.9131	66.62	0.5874	0.7344
RealSR	OSDiff-1s	25.15	0.7341	0.2920	0.2128	123.48	5.6471	69.10	0.6326	0.6687
	AddSR-1s	24.79	0.7077	0.3091	0.2191	132.05	5.5440	66.18	0.6098	0.5722
	SinSR-1s	26.27	0.7351	0.3217	0.2341	137.59	6.2964	60.76	0.5418	0.6163
	Ours-1s	24.81	0.7172	0.2743	0.2104	114.45	5.1298	71.19	0.6347	0.7160
DIV2K-Val	OSDiff-1s	23.72	0.6109	0.2942	0.1975	26.34	4.7089	67.96	0.6131	0.6681
	AddSR-1s	23.26	0.5902	0.3623	0.2123	29.68	4.7610	63.39	0.5657	0.5734
	SinSR-1s	24.41	0.6018	0.3262	0.2068	35.55	5.9981	62.95	0.5430	0.6501
	Ours-1s	23.02	0.5808	0.2673	0.1821	29.16	4.3244	71.69	0.6192	0.7416

Table 2. Quantitative comparison with state-of-the-art multi-step methods across both synthetic and real-world benchmarks. The number of diffusion inference steps is indicated by ‘s’. The best and second best results of each metric are highlighted in **red** and **blue**, respectively.

Datasets	Method	PSNR \uparrow	SSIM \uparrow	LPIPS \downarrow	DISTS \downarrow	FID \downarrow	NIQE \downarrow	MUSIQ \uparrow	MANIQA \uparrow	CLIPQA \uparrow
DRealSR	StableSR-200s	28.04	0.7454	0.3279	0.2272	144.15	6.5999	58.53	0.5603	0.6250
	DiffBIR-50s	25.93	0.6525	0.4518	0.2761	177.04	6.2324	65.66	0.6296	0.6860
	SeeSR-50s	28.14	0.7712	0.3141	0.2297	146.95	6.4632	64.74	0.6022	0.6893
	SUPIR-50s	25.09	0.6460	0.4243	0.2795	169.48	7.3918	58.79	0.5471	0.6749
	PASD-20s	27.79	0.7495	0.3579	0.2524	171.03	6.7661	63.23	0.5919	0.6242
	ResShift-15s	28.69	0.7874	0.3525	0.2541	176.77	7.8762	52.40	0.4756	0.5413
	AddSR-4s	26.72	0.7124	0.3982	0.2711	164.12	7.6689	66.33	0.6257	0.7226
	Ours-1s	27.77	0.7559	0.2967	0.2136	134.98	5.9131	66.62	0.5874	0.7344
RealSR	StableSR-200s	24.62	0.7041	0.3070	0.2156	128.54	5.7817	65.48	0.6223	0.6198
	DiffBIR-50s	24.24	0.6650	0.3469	0.2300	134.56	5.4932	68.35	0.6544	0.6961
	SeeSR-50s	25.21	0.7216	0.3003	0.2218	125.10	5.3978	69.69	0.6443	0.6671
	SUPIR-50s	23.65	0.6620	0.3541	0.2488	130.38	6.1099	62.09	0.5780	0.6707
	PASD-20s	25.68	0.7273	0.3144	0.2304	134.18	5.7616	68.33	0.6323	0.5783
	ResShift-15s	26.39	0.7567	0.3158	0.2432	149.59	6.8746	60.22	0.5419	0.5496
	AddSR-4s	23.33	0.6400	0.3925	0.2626	154.22	5.8959	71.49	0.6826	0.7225
	Ours-1s	24.81	0.7172	0.2743	0.2104	114.45	5.1298	71.19	0.6347	0.7160
DIV2K-Val	StableSR-200s	23.27	0.5722	0.3111	0.2046	24.95	4.7737	65.78	0.6164	0.6753
	DiffBIR-50s	23.13	0.5717	0.3469	0.2108	33.93	4.6056	68.54	0.6360	0.7125
	SeeSR-50s	23.73	0.6057	0.3198	0.1953	25.81	4.8322	68.49	0.6198	0.6899
	SUPIR-50s	22.13	0.5279	0.3919	0.2312	31.40	5.6767	63.86	0.5903	0.7146
	PASD-20s	24.00	0.6041	0.3779	0.2305	39.12	4.8587	67.36	0.6121	0.6327
	ResShift-15s	24.71	0.6234	0.3473	0.2253	42.01	6.3615	60.63	0.5283	0.5962
	AddSR-4s	22.16	0.5280	0.4053	0.2360	35.41	5.2584	70.99	0.6596	0.7593
	Ours-1s	23.02	0.5808	0.2673	0.1821	29.16	4.3244	71.69	0.6192	0.7416

distributions over strict pixel fidelity. We anticipate the development of better full-reference metrics in the future to assess advanced Real-ISR methods. Refer to the supplementary material for detailed visual comparisons.

Qualitative Comparisons. Fig. 7 presents visual comparisons of different Real-ISR methods. As shown in the results of multi-step methods, SeeSR leverages degradation-aware semantic cues to incorporate image generation priors, but it tends to produce over-smoothed textures in some cases. SUPIR demonstrates notably robust generative capa-

bilities. However, the excessive generation of fine details can result in outputs that appear less natural (e.g., adding unnecessary wrinkles around the eyes of a young girl). Under more realistic degradation conditions, PASD finds it difficult to recover the appropriate content, indicating limited robustness. Among single-step methods, SinSR tends to produce artifacts, likely due to its base model, ResShift, being trained from scratch without adequate exposure to real-world priors, which leads to inferior image restoration quality. AddSR produces over-smoothed results when using its

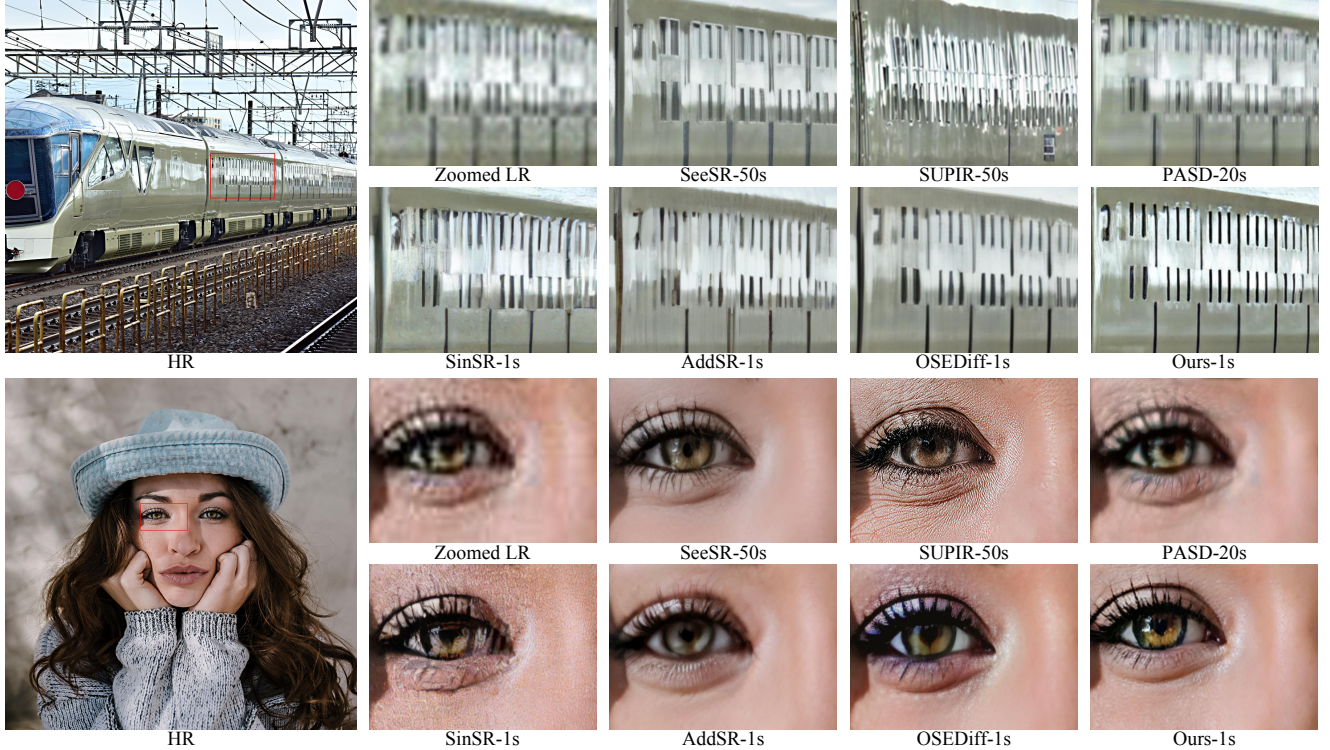


Figure 7. Visual comparisons of different Real-ISR methods. Please zoom in for a better view.

Table 3. Comparison of computational complexity across different diffusion model-based methods. Performance is measured on an A100 GPU using 512×512 input images, excluding model weight and data loading time.

	StableSR	DiffBIR	SeeSR	SUPIR	PASD	ResShift	AddSR	AddSR	SinSR	OSEDiff	Ours
Inference Step	200	50	50	50	20	15	4	1	1	1	1
Inference Time	12.4151	7.9637	5.8167	16.8704	4.8441	0.7546	1.0199	0.5043	0.1424	0.1650	0.1362

1-step model. OSEDiff demonstrates better restoration performance than SinSR and AddSR; however, it may fall short in terms of authenticity and naturalness, particularly in recovering fine details. In contrast, our method effectively generates rich textures and realistic details with enhanced sharpness and contrast. Additional visual comparisons and results are provided in the supplementary material.

Complexity Comparisons We assess the computational complexity of the state-of-the-art DM-based Real-ISR methods, as detailed in Tab. 3, with a focus on inference time. Each method is benchmarked on an A100 GPU using input images of size 512×512 pixels. We disregarded the loading time for model weights and data. The main computation time consists of: (1) text extraction time (if a text extractor is used); (2) text encoder computation time (if applicable); (3) VAE encoding and decoding time; and (4) denoising network execution time. It is evident that TSD-SR holds a substantial advantage in inference speed compared to multi-step models. Specifically, TSD-SR is over 120× faster than SUPIR, 90× faster than StableSR, approximately

50× faster than DiffBIR, over 40× faster than SeeSR, more than 35× faster than PASD, and 4× faster than ResShift. When compared with existing one-step models, our method achieves the fastest inference times. This advantage is attributed to directly denoising from LQ data and employing a fixed prompt.

4.3. User Study

We conduct a user study comparing our method with three other diffusion-based one-step super-resolution methods. To ensure a comprehensive evaluation, we selected images from five categories—human faces, buildings, animals, vegetation, and characters. A total of 50 participants took part in the voting process. Participants were instructed to select the best restoration results based on similarity to the HQ image, structural similarity to the LQ image, and realism of textures and details. The results in Fig. 8 indicate that our method received a 69.2% approval rate from users. Specifically, our method achieved 57.6% in Animals, 70.0% in Buildings, 68.8% in Human Faces, 65.2% in Vegetation,

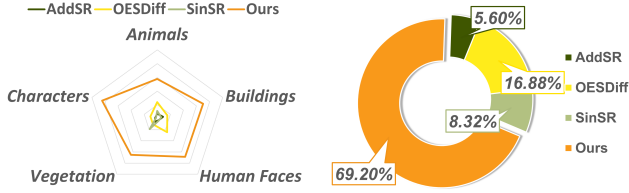


Figure 8. Results of our user study. Left: Category-based user preference radar chart, showing that our model received the highest favor across all categories. Right: User preference pie chart, illustrating that our approach garnered a 69.2% user satisfaction rating.

Table 4. Ablation study of Target Score Matching loss and Distribution-Aware Sampling Module.

Datasets	Method	LPIPS ↓	DISTS ↓	FID ↓	MUSIQ ↑	MANIQA ↑	CLIPQA ↑
DRealSR	w/o TSM	0.3176	0.2327	139.67	63.90	0.5749	0.6958
	w/o DASM	0.3097	0.2311	143.97	63.56	0.5812	0.7123
	Full	0.2967	0.2136	134.98	66.62	0.5874	0.7344
RealSR	w/o TSM	0.2934	0.2397	117.15	68.56	0.6338	0.6987
	w/o DASM	0.2873	0.2273	123.51	69.05	0.6273	0.7031
	Full	0.2743	0.2104	114.45	71.19	0.6347	0.7160

and 84.4% in Characters, surpassing those of other methods.

4.4. Ablation Study

Effectiveness of TSM and DASM. To validate the effectiveness of the TSM loss and DASM, we conduct ablation studies by removing each component separately. We select LPIPS, DISTS, MUSIQ, MANIQA, and CLIPQA for comparison, as these metrics are critical for image quality assessment. Additionally, FID is used to evaluate distribution similarity. The results are presented in Tab. 4. From the results, we draw the following conclusions: (1) The absence of TSM loss and DASM negatively impacts performance across both reference-based metrics (LPIPS, DISTS) and no-reference metrics (MUSIQ, MANIQA, and CLIPQA). The FID metric is also adversely affected, indicating a decline in distribution fidelity. (2) The lack of TSM leads to a significant decrease in LPIPS, DISTS, MUSIQ, and CLIPQA, possibly due to unreliable directions in VSD leading to unrealistic generations. (3) The absence of DASM results in a decline in FID, MUSIQ, and CLIPQA, possibly due to suboptimal detail optimization.

Base model for fairer comparison. To validate the effectiveness of our method across different versions of SD models, we conduct additional experiments on SD2-base and SD2.1-base models, as shown in Tab. 5. The performance is evaluated on the DRealSR test dataset [52]. Our method demonstrates superior performance compared to other one-step SR methods, including OSediff [53] and

Table 5. Fair comparison using the same base model to validate TSD-SR

Model	Base Model	LPIPS ↓	DISTS ↓	NIQE ↓	MUSIQ ↑	CLIPQA ↑
AddSR	SD2-base	0.3196	0.2242	6.9321	60.85	0.6188
Ours	SD2-base	0.3040	0.2234	6.2202	65.14	0.6935
OSediff	SD2.1-base	0.2968	0.2162	6.4471	64.69	0.6958
Ours	SD2.1-base	0.2943	0.2115	5.7934	65.41	0.7109

Table 6. Ablation studies for hyperparameter N and s .

N	s	LPIPS ↓	DISTS ↓	FID ↓	MUSIQ ↑	MANIQA ↑	CLIPQA ↑
2	50	0.3104	0.2327	137.64	64.49	0.5717	0.7118
4	50	0.2967	0.2136	134.98	66.62	0.5874	0.7344
8	50	0.3421	0.2633	151.64	65.73	0.5875	0.7227
4	25	0.3063	0.2201	130.74	66.19	0.5828	0.7269
4	100	0.3176	0.2230	135.54	65.23	0.5782	0.7024

AddSR [55]. Specifically, our SD2-base model outperforms single-step AddSR across all perceptual reference and no-reference metrics, particularly excelling in NIQE [64], MUSIQ [22], and CLIPQA [44]. Meanwhile, our SD2.1-base model shows comparable or better performance than OSediff across various metrics, with notable improvements in NIQE and CLIPQA.

Parameters N and s in DASM. We compare performance under different combinations of N and s in Tab. 6. The evaluation is conducted on the DRealSR test dataset. In our setting, N is set to 4 and s to 50 (highlighted in bold in the table). Performance degrades when N is either larger or smaller, possibly due to its effect on regularization strength. Since DASM is computationally expensive, we prefer a smaller N . After balancing training time and performance, we select $N = 4$ as the final value. Smaller values of s yield similar performance, while larger values degrade image quality. Experimental results suggest that choosing s between 25 and 75 achieves better overall performance.

5. Conclusion and Limitation

We propose TSD-SR, an effective one-step model for RealISR based on diffusion priors. TSD-SR utilizes TSD to enhance the realism of images generated by the distillation model, and leverages DASM to sample distribution-based noisy latents and accumulate their gradients, thereby improving detail recovery. Our experiments demonstrate that TSD-SR outperforms existing one-step RealISR models in both restoration quality and inference speed.

limitations. Although our model achieves excellent inference speed and restoration performance, it still contains significantly more parameters compared to previous GAN- or non-diffusion-based methods. In future work, we plan to apply pruning or quantization techniques to compress the model, aiming to develop a lightweight and efficient RealISR solution.

6. Acknowledgment

This work was supported by National Natural Science Foundation of China (62293554, U2336212), Zhejiang Provincial Natural Science Foundation of China (LD24F020007), National Key R&D Program of China (SQ2023AAA01005), Ningbo Innovation “Yongjiang 2035” Key Research and Development Programme (2024Z292), and Young Elite Scientists Sponsorship Program by CAST (2023QNRC001).

Supplementary Material

In this Supplementary Material, we provide additional details, including the comparison with GAN-based methods in Appendix A, more visual comparisons in Appendix B, comparisons of full-reference metrics and human preference in Appendix C, theory of Target Score Matching in Appendix D and algorithm in Appendix E. We conduct these additional comparisons and analyses to validate the effectiveness of TSD-SR.

A. Comparison with GAN-based Methods

We compare our method with GAN-based approaches in Tab. 7. While the GAN methods show advantages in full-reference metrics such as PSNR and SSIM, our model outperforms them across all no-reference metrics. Prior studies have highlighted the limitations of PSNR and SSIM for evaluating image super-resolution performance [55, 61]. Their effectiveness in assessing image fidelity in complex degradation scenarios remains debatable, as pixel-level misalignment often arises when restoring severely degraded images. However, no-reference metrics evaluate image quality based solely on the individual image, without requiring alignment with the ground truth. Therefore, in more complex and realistic degradation scenarios, they may offer a more appropriate evaluation of super-resolution results. In Appendix C, we further provide a visual comparison between full-reference metrics and human preferences, and in Fig. 9, we present a visual comparison with GAN-based methods. From these visualizations, it is evident that our model produces more realistic texture details than the GAN-based approaches.

B. More Visual Comparisons

In Figs. 10 to 12, we provide additional visual comparisons with other diffusion-based methods. These examples further demonstrate the robust restoration capabilities of TSD-SR and the high quality of the restored images.

C. Comparisons of Full-reference Metrics and Human Preference

We present additional comparative experiments in Figure 13 to demonstrate the limitations of PSNR and SSIM in assessing image fidelity under complex degradation scenarios. As observed, GAN-based methods with higher PSNR and SSIM scores tend to produce over-smoothed or fragmented textures, raising concerns about their realism and perceptual fidelity. In contrast, our approach sacrifices some PSNR and SSIM performance to achieve more natural detail restoration, resulting in enhanced realism and broader perceptual acceptance. An additional user study shows that 90.28% of participants prefer our results over those of methods with higher PSNR and SSIM scores.

D. Theory of Target Score Matching

The core idea of Target Score Matching (TSM) is that for samples drawn from the same distribution, the real scores predicted by the Teacher Model should be close to each other. Thus, we minimize the MSE loss between the Teacher Model’s predictions on \hat{z}_t and z_t by

$$\begin{aligned} \mathcal{L}_{\text{MSE}}(\hat{z}, z, c_y) \\ = \mathbb{E}_{t, \epsilon} [w(t) \|\epsilon_\psi(\hat{z}_t; t, c_y) - \epsilon_\psi(z_t; t, c_y)\|_2^2] \end{aligned} \quad (10)$$

where the expectation of the gradient is computed across all diffusion timesteps $t \in \{1, \dots, T\}$ and $\epsilon \sim \mathcal{N}(0, I)$.

Table 7. Quantitative comparison with GAN-based methods on both synthetic and real-world benchmarks. The best results of each metric are highlighted in red.

Datasets	Method	PSNR \uparrow	SSIM \uparrow	LPIPS \downarrow	DISTS \downarrow	FID \downarrow	NIQE \downarrow	MUSIQ \uparrow	MANIQA \uparrow	CLIPQA \uparrow
DRealSR	BSRGAN	28.70	0.8028	0.2858	0.2143	155.61	6.5408	57.15	0.4847	0.5091
	Real-ESRGAN	28.61	0.8051	0.2818	0.2088	147.66	6.7001	54.27	0.4888	0.4521
	LDL	28.20	0.8124	0.2791	0.2127	155.51	7.1448	53.94	0.4894	0.4476
	FeMASR	26.87	0.7569	0.3156	0.2238	157.72	5.9067	53.70	0.4413	0.5633
	Ours	27.77	0.7559	0.2967	0.2136	134.98	5.9131	66.62	0.5874	0.7344
RealSR	BSRGAN	26.38	0.7651	0.2656	0.2123	141.24	5.6431	63.28	0.5425	0.5114
	Real-ESRGAN	26.65	0.7603	0.2726	0.2065	136.29	5.8471	60.45	0.5507	0.4518
	LDL	25.28	0.7565	0.2750	0.2119	142.74	5.9880	60.92	0.5494	0.4559
	FeMASR	25.06	0.7356	0.2936	0.2285	141.01	5.7696	59.05	0.4872	0.5405
	Ours	24.81	0.7172	0.2743	0.2104	114.45	5.1298	71.19	0.6347	0.7160
DIV2K-Val	BSRGAN	24.58	0.6269	0.3502	0.2280	49.55	4.7501	61.68	0.4979	0.5386
	Real-ESRGAN	24.02	0.6387	0.3150	0.2123	38.87	4.8271	60.38	0.5401	0.5251
	LDL	23.83	0.6344	0.3256	0.2227	42.28	4.8555	60.04	0.5328	0.5180
	FeMASR	22.45	0.5858	0.3370	0.2205	41.97	4.8679	57.94	0.4787	0.5769
	Ours	23.02	0.5808	0.2673	0.1821	29.16	4.3244	71.69	0.6192	0.7416

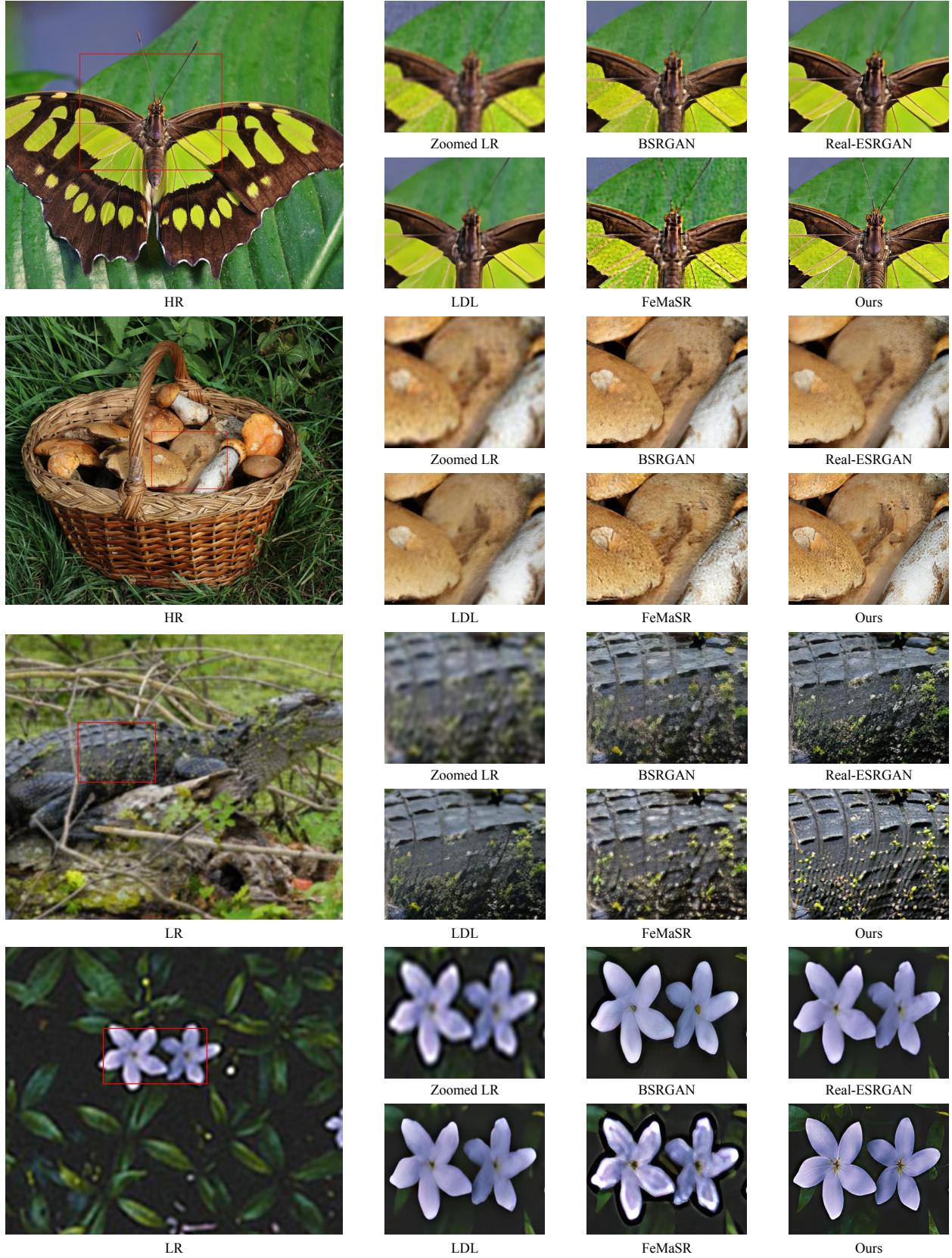


Figure 9. Qualitative comparisons between TSD-SR and GAN-based Real-ISR methods. Please zoom in for a better view.

To understand the difficulties of this approach, consider the gradient of

$$\nabla_{\theta} \mathcal{L}_{\text{MSE}}(\hat{\mathbf{z}}, \mathbf{z}, c_y) = \mathbb{E}_{t, \epsilon} \left[w(t) \cdot \underbrace{\frac{\partial \epsilon_{\psi}(\hat{\mathbf{z}}_t; t, c_y)}{\partial \hat{\mathbf{z}}_t}}_{\text{Diffusion Jacobian}} \underbrace{\left(\underbrace{\epsilon_{\psi}(\hat{\mathbf{z}}_t; t, c_y) - \epsilon_{\psi}(\mathbf{z}_t; t, c_y)}_{\text{Prediction Residual}} \right) \frac{\partial \hat{\mathbf{z}}}{\partial \theta}}_{\text{Generator Jacobian}} \right] \quad (11)$$

where we absorb $\frac{\partial \hat{\mathbf{z}}_t}{\partial \hat{\mathbf{z}}}$ and the other constant into $w(t)$. The computation of the Diffusion Jacobian term is computationally demanding, as it necessitates backpropagation through the Teacher Model. DreamFusion [36] found that this term struggles with small noise levels due to its training to approximate the scaled Hessian of marginal density. This work also demonstrated that omitting the Diffusion Jacobian term leads to an effective gradient for optimizing. Similar to their approach, we update Eq. (11) by omitting Diffusion Jacobian:

$$\nabla_{\theta} \mathcal{L}_{\text{TSM}}(\hat{\mathbf{z}}, \mathbf{z}, c_y) = \mathbb{E}_{t, \epsilon} \left[w(t) \underbrace{(\epsilon_{\psi}(\hat{\mathbf{z}}_t; c_y, t) - \epsilon_{\psi}(\mathbf{z}_t; c_y, t))}_{\text{Prediction Residual}} \underbrace{\frac{\partial \hat{\mathbf{z}}}{\partial \theta}}_{\text{Generator Jacobian}} \right] \quad (12)$$

The effectiveness of the method can be proven by starting from the KL divergence. We can use a Sticking-the-Landing [39] style gradient by thinking of $\epsilon_{\psi}(\mathbf{z}_t; c_y, t)$ as a control variate for $\hat{\epsilon}$. For detailed proof, refer to Appendix 4 of DreamFusion [36]. It demonstrates that the gradient of this loss yields the same updates as optimizing the training loss \mathcal{L}_{MSE} Eq. (10), excluding the Diffusion Jacobian term.

Compared with the VSD loss, we find that the term ‘‘Prediction Residual’’ has changed, and the two losses are similar in the gradient update mode. Specifically, we find that VSD employs identical inputs for both the Teacher and

LoRA models to compute the gradient, while here TSM uses high-quality and suboptimal inputs for the Teacher Model. The losses are related to each other through $\epsilon_{\phi}(\hat{\mathbf{z}}_t; t, c_y)$.

E. Algorithm

Algorithm 1 details our TSD-SR training procedure. We use classifier-free guidance (cfg) for the Teacher Model and the LoRA Model. The cfg weight is set to 7.5.

References

- [1] Eirikur Agustsson and Radu Timofte. Ntire 2017 challenge on single image super-resolution: Dataset and study. In *Proceedings of the IEEE conference on computer vision and pattern recognition workshops*, pages 126–135, 2017. 6
- [2] Martin Arjovsky, Soumith Chintala, and Léon Bottou. Wasserstein generative adversarial networks. In *International conference on machine learning*, pages 214–223. PMLR, 2017. 1, 2
- [3] Yochai Blau and Tomer Michaeli. The perception-distortion tradeoff. In *Proceedings of the IEEE conference on computer vision and pattern recognition*, pages 6228–6237, 2018. 6
- [4] Jianrui Cai, Hui Zeng, Hongwei Yong, Zisheng Cao, and Lei Zhang. Toward real-world single image super-resolution: A new benchmark and a new model. In *Proceedings of the IEEE/CVF international conference on computer vision*, pages 3086–3095, 2019. 6
- [5] Chaofeng Chen, Xinyu Shi, Yipeng Qin, Xiaoming Li, Xiaoguang Han, Tao Yang, and Shihui Guo. Real-world blind super-resolution via feature matching with implicit high-resolution priors. In *Proceedings of the 30th ACM International Conference on Multimedia*, pages 1329–1338, 2022. 6
- [6] Hanqing Chen, Yunhe Wang, Tianyu Guo, Chang Xu, Yiping Deng, Zhenhua Liu, Siwei Ma, Chunjing Xu, Chao Xu, and Wen Gao. Pre-trained image processing transformer. In *Proceedings of the IEEE/CVF conference on computer vision and pattern recognition*, pages 12299–12310, 2021. 1



Figure 10. Qualitative comparisons between TSD-SR and different diffusion-based methods. Our method can effectively restore the texture and details of the corresponding object under challenging degradation conditions. Please zoom in for a better view.



Figure 11. Qualitative comparisons between TSD-SR and different diffusion-based methods. Our method can effectively restore the texture and details of the corresponding object under challenging degradation conditions. Please zoom in for a better view.

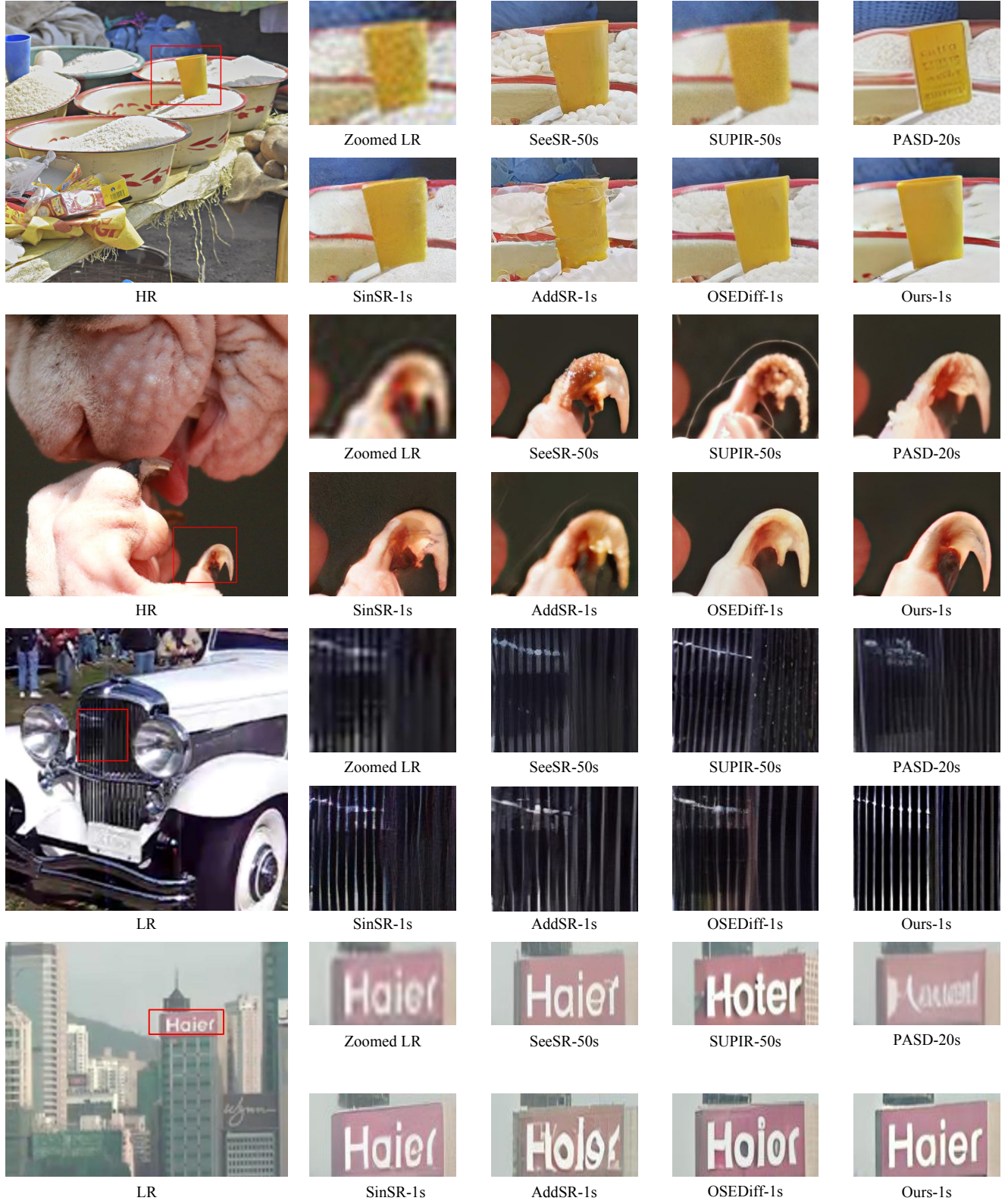


Figure 12. Qualitative comparisons between TSD-SR and different diffusion-based methods. Our method can effectively restore the texture and details of the corresponding object under challenging degradation conditions. Please zoom in for a better view.

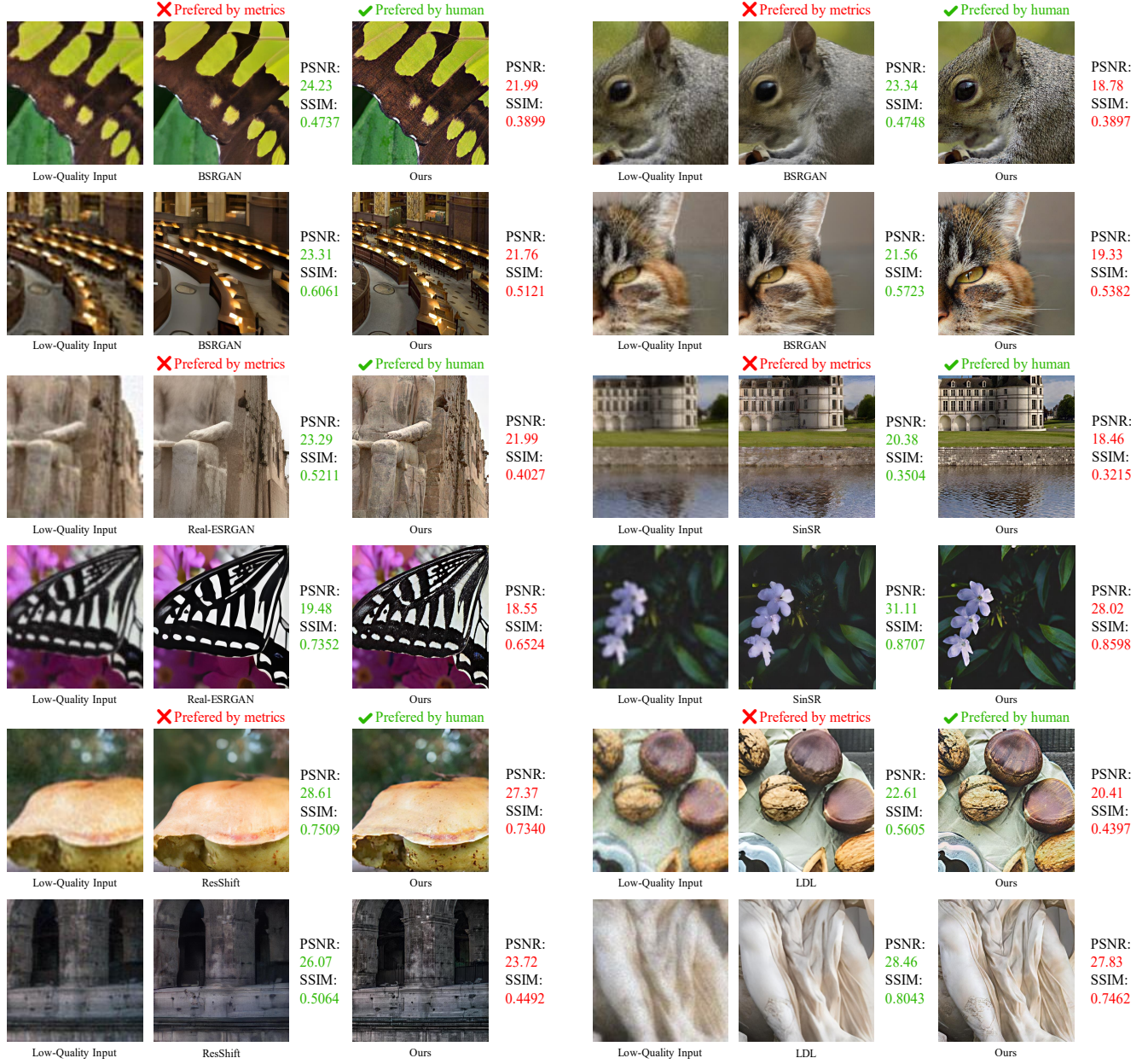


Figure 13. Comparisons between full-reference metric assessments and human visual preference. Despite scoring lower on full-reference metrics, TSD-SR generates images that align with human preference.

- [7] Keyan Ding, Kede Ma, Shiqi Wang, and Eero P Simoncelli. Image quality assessment: Unifying structure and texture similarity. *IEEE transactions on pattern analysis and machine intelligence*, 44(5):2567–2581, 2020. 2, 6
- [8] Chao Dong, Chen Change Loy, Kaiming He, and Xiaoou Tang. Learning a deep convolutional network for image super-resolution. In *Computer Vision–ECCV 2014: 13th European Conference, Zurich, Switzerland, September 6–12, 2014, Proceedings, Part IV 13*, pages 184–199. Springer, 2014. 1
- [9] Chao Dong, Chen Change Loy, Kaiming He, and Xiaoou

Tang. Image super-resolution using deep convolutional networks. *IEEE transactions on pattern analysis and machine intelligence*, 38(2):295–307, 2015. 1

- [10] Patrick Esser, Sumith Kulal, Andreas Blattmann, Rahim Entezari, Jonas Müller, Harry Saini, Yam Levi, Dominik Lorenz, Axel Sauer, Frederic Boesel, et al. Scaling rectified flow transformers for high-resolution image synthesis. In *Forty-first International Conference on Machine Learning*, 2024. 2, 6
- [11] Ian Goodfellow, Jean Pouget-Abadie, Mehdi Mirza, Bing Xu, David Warde-Farley, Sherjil Ozair, Aaron Courville, and

Algorithm 1: TSD-SR Training Procedure

Input: $\mathcal{D} = \{x_L, x_H, c_y\}$, pre-trained Teacher Diffusion Model including VAE encoder E_ψ , denoising network ϵ_ψ and VAE decoder D_ψ , the number of iterations N and step size s of DASM.

Output: Trained one-step Student Model G_θ .

```
1 Initialize Student Model  $G_\theta$ , including  $E_\theta \leftarrow E_\psi$  with trainable LoRA,  $\epsilon_\theta \leftarrow \epsilon_\psi$  with trainable LoRA,  $D_\theta \leftarrow D_\psi$ .
2 Initialize LoRA diffusion network  $\epsilon_\phi \leftarrow \epsilon_\psi$  with trainable LoRA.
3 while train do
4   Sample  $(x_L, x_H, c_y) \sim \mathcal{D}$ 
   /* Network forward */
5    $\hat{z} \leftarrow \epsilon_\theta(E_\theta(x_L)), z \leftarrow E_\psi(x_H)$ 
6    $\hat{x}_H \leftarrow D_\psi(\hat{z})$ 
   /* Compute reconstruction loss */
7    $\mathcal{L}_{Rec} \leftarrow LPIPS(\hat{x}_H, x_H)$ 
   /* Compute regularization loss */
8   Sample  $\epsilon$  from  $\mathcal{N}(0, I)$ ,  $t$  from  $\{50, \dots, 950\}$ 
9    $\sigma_t \leftarrow \text{FlowMatchingScheduler}(t)$ 
10   $\hat{z}_t \leftarrow \sigma_t \epsilon + (1 - \sigma_t) \hat{z}, z_t \leftarrow \sigma_t \epsilon + (1 - \sigma_t) z$ 
11   $\mathcal{L}_{Reg} \leftarrow \mathcal{L}_{TSD}(\hat{z}_t, z_t, c_y)$  // Eq. (5)
12  for  $i \leftarrow 1$  to  $N$  do
13     $cur \leftarrow t - i \cdot s$ 
14     $pre \leftarrow t - i \cdot s + s$ 
15     $\sigma_{cur} \leftarrow \text{FlowMatchingScheduler}(cur)$ 
16     $\sigma_{pre} \leftarrow \text{FlowMatchingScheduler}(pre)$ 
17     $\hat{z}_{cur} \leftarrow \hat{z}_{pre} + (\sigma_{cur} - \sigma_{pre}) \cdot \epsilon_\phi(\hat{z}_{pre}; pre, c_y)$  // Eq. (6)
18     $z_{cur} \leftarrow z_{pre} + (\sigma_{cur} - \sigma_{pre}) \cdot \epsilon_\psi(z_{pre}; pre, c_y)$ 
19     $\mathcal{L}_{Reg} += weight \cdot \mathcal{L}_{TSD}(\hat{z}_{cur}, z_{cur}, c_y)$ 
20  end
21   $\mathcal{L}_G \leftarrow \mathcal{L}_{Rec} + \gamma \mathcal{L}_{Reg}$ 
22  Update  $\theta$  with  $\mathcal{L}_G$ 
   /* Compute diffusion loss for LoRA Model */
23  Sample  $\epsilon$  from  $\mathcal{N}(0, I)$ ,  $t$  from  $\{50, \dots, 950\}$ 
24   $\sigma_t \leftarrow \text{FlowMatchingScheduler}(t)$ 
25   $\hat{z}_t \leftarrow \sigma_t \epsilon + (1 - \sigma_t) stopgrad(\hat{z})$ 
26   $\mathcal{L}_{Lora} \leftarrow \mathcal{L}_{Diff}(\hat{z}_t, c_y)$  // Eq. (9)
27  Update  $\phi$  with  $\mathcal{L}_{Lora}$ 
28 end
```

Yoshua Bengio. Generative adversarial nets. *Advances in neural information processing systems*, 27, 2014. 1

- [12] Jianping Gou, Baosheng Yu, Stephen J Maybank, and Dacheng Tao. Knowledge distillation: A survey. *International Journal of Computer Vision*, 129(6):1789–1819, 2021. 2
- [13] Xiangyu He and Jian Cheng. Revisiting l1 loss in super-resolution: a probabilistic view and beyond. *arXiv preprint arXiv:2201.10084*, 2022. 4
- [14] Martin Heusel, Hubert Ramsauer, Thomas Unterthiner, Bernhard Nessler, and Sepp Hochreiter. Gans trained by a two time-scale update rule converge to a local nash equilibrium. *Advances in neural information processing systems*, 30, 2017. 6
- [15] Geoffrey Hinton. Distilling the knowledge in a neural net-

work. *arXiv preprint arXiv:1503.02531*, 2015. 2

- [16] Jonathan Ho and Tim Salimans. Classifier-free diffusion guidance. *arXiv preprint arXiv:2207.12598*, 2022. 2
- [17] Jonathan Ho, Ajay Jain, and Pieter Abbeel. Denoising diffusion probabilistic models. *Advances in neural information processing systems*, 33:6840–6851, 2020. 1
- [18] Andrew G Howard. Mobilenets: Efficient convolutional neural networks for mobile vision applications. *arXiv preprint arXiv:1704.04861*, 2017. 2
- [19] Edward J Hu, Yelong Shen, Phillip Wallis, Zeyuan Allen-Zhu, Yuanzhi Li, Shean Wang, Lu Wang, and Weizhu Chen. Lora: Low-rank adaptation of large language models. *arXiv preprint arXiv:2106.09685*, 2021. 3
- [20] Tero Karras, Samuli Laine, and Timo Aila. A style-based generator architecture for generative adversarial networks.

- In *Proceedings of the IEEE/CVF conference on computer vision and pattern recognition*, pages 4401–4410, 2019. 6
- [21] Bahjat Kawar, Michael Elad, Stefano Ermon, and Jiaming Song. Denoising diffusion restoration models. *Advances in Neural Information Processing Systems*, 35:23593–23606, 2022. 1
- [22] Junjie Ke, Qifei Wang, Yilin Wang, Peyman Milanfar, and Feng Yang. Musiq: Multi-scale image quality transformer. In *Proceedings of the IEEE/CVF international conference on computer vision*, pages 5148–5157, 2021. 6, 9
- [23] Jiwon Kim, Jung Kwon Lee, and Kyoung Mu Lee. Accurate image super-resolution using very deep convolutional networks. In *Proceedings of the IEEE conference on computer vision and pattern recognition*, pages 1646–1654, 2016. 1
- [24] Diederik P Kingma. Auto-encoding variational bayes. *arXiv preprint arXiv:1312.6114*, 2013. 6
- [25] Solomon Kullback and Richard A Leibler. On information and sufficiency. *The annals of mathematical statistics*, 22(1): 79–86, 1951. 3
- [26] Christian Ledig, Lucas Theis, Ferenc Huszár, Jose Caballero, Andrew Cunningham, Alejandro Acosta, Andrew Aitken, Alykhan Tejani, Johannes Totz, Zehan Wang, et al. Photo-realistic single image super-resolution using a generative adversarial network. In *Proceedings of the IEEE conference on computer vision and pattern recognition*, pages 4681–4690, 2017. 1, 2
- [27] Yawei Li, Kai Zhang, Jingyun Liang, Jiezhang Cao, Ce Liu, Rui Gong, Yulun Zhang, Hao Tang, Yun Liu, Denis Deman-dolx, et al. Lsdrr: A large scale dataset for image restoration. In *Proceedings of the IEEE/CVF Conference on Computer Vision and Pattern Recognition*, pages 1775–1787, 2023. 6
- [28] Jie Liang, Hui Zeng, and Lei Zhang. Details or artifacts: A locally discriminative learning approach to realistic image super-resolution. In *Proceedings of the IEEE/CVF Conference on Computer Vision and Pattern Recognition*, pages 5657–5666, 2022. 6
- [29] Xinqi Lin, Jingwen He, Ziyang Chen, Zhaoyang Lyu, Bo Dai, Fanghua Yu, Wanli Ouyang, Yu Qiao, and Chao Dong. Diff-bir: Towards blind image restoration with generative diffusion prior. *arXiv preprint arXiv:2308.15070*, 2023. 1, 2, 6
- [30] I Loshchilov. Decoupled weight decay regularization. *arXiv preprint arXiv:1711.05101*, 2017. 6
- [31] Simian Luo, Yiqin Tan, Longbo Huang, Jian Li, and Hang Zhao. Latent consistency models: Synthesizing high-resolution images with few-step inference. *arXiv preprint arXiv:2310.04378*, 2023. 2
- [32] Xiaotong Luo, Yuan Xie, Yanyun Qu, and Yun Fu. Skipdiff: Adaptive skip diffusion model for high-fidelity perceptual image super-resolution. In *Proceedings of the AAAI Conference on Artificial Intelligence*, pages 4017–4025, 2024. 6
- [33] Mehdi Mirza. Conditional generative adversarial nets. *arXiv preprint arXiv:1411.1784*, 2014. 1
- [34] Thuan Hoang Nguyen and Anh Tran. Swiftbrush: One-step text-to-image diffusion model with variational score distillation. In *Proceedings of the IEEE/CVF Conference on Computer Vision and Pattern Recognition*, pages 7807–7816, 2024. 2
- [35] Dustin Podell, Zion English, Kyle Lacey, Andreas Blattmann, Tim Dockhorn, Jonas Müller, Joe Penna, and Robin Rombach. Sdxl: Improving latent diffusion models for high-resolution image synthesis. *arXiv preprint arXiv:2307.01952*, 2023. 2
- [36] Ben Poole, Ajay Jain, Jonathan T Barron, and Ben Mildenhall. Dreamfusion: Text-to-3d using 2d diffusion. *arXiv preprint arXiv:2209.14988*, 2022. 3, 13
- [37] Alec Radford. Unsupervised representation learning with deep convolutional generative adversarial networks. *arXiv preprint arXiv:1511.06434*, 2015. 1
- [38] Aditya Ramesh, Prafulla Dhariwal, Alex Nichol, Casey Chu, and Mark Chen. Hierarchical text-conditional image generation with clip latents. *arXiv preprint arXiv:2204.06125*, 1 (2):3, 2022. 2
- [39] Geoffrey Roeder, Yuhuai Wu, and David K Duvenaud. Sticking the landing: Simple, lower-variance gradient estimators for variational inference. *Advances in Neural Information Processing Systems*, 30, 2017. 13
- [40] Robin Rombach, Andreas Blattmann, Dominik Lorenz, Patrick Esser, and Björn Ommer. High-resolution image synthesis with latent diffusion models. In *Proceedings of the IEEE/CVF conference on computer vision and pattern recognition*, pages 10684–10695, 2022. 1, 2
- [41] Axel Sauer, Dominik Lorenz, Andreas Blattmann, and Robin Rombach. Adversarial diffusion distillation. *arXiv preprint arXiv:2311.17042*, 2023. 2
- [42] Yang Song, Jascha Sohl-Dickstein, Diederik P Kingma, Abhishek Kumar, Stefano Ermon, and Ben Poole. Score-based generative modeling through stochastic differential equations. *arXiv preprint arXiv:2011.13456*, 2020. 1
- [43] Radu Timofte, Eirikur Agustsson, Luc Van Gool, Ming-Hsuan Yang, and Lei Zhang. Ntire 2017 challenge on single image super-resolution: Methods and results. In *Proceedings of the IEEE conference on computer vision and pattern recognition workshops*, pages 114–125, 2017. 6
- [44] Jianyi Wang, Kelvin CK Chan, and Chen Change Loy. Exploring clip for assessing the look and feel of images. In *Proceedings of the AAAI Conference on Artificial Intelligence*, pages 2555–2563, 2023. 6, 9
- [45] Jianyi Wang, Zongsheng Yue, Shangchen Zhou, Kelvin CK Chan, and Chen Change Loy. Exploiting diffusion prior for real-world image super-resolution. *International Journal of Computer Vision*, pages 1–21, 2024. 2, 6
- [46] Xintao Wang, Ke Yu, Shixiang Wu, Jinjin Gu, Yihao Liu, Chao Dong, Yu Qiao, and Chen Change Loy. Esrgan: Enhanced super-resolution generative adversarial networks. In *Proceedings of the European conference on computer vision (ECCV) workshops*, pages 0–0, 2018. 2, 3
- [47] Xintao Wang, Liangbin Xie, Chao Dong, and Ying Shan. Real-esrgan: Training real-world blind super-resolution with pure synthetic data. In *Proceedings of the IEEE/CVF international conference on computer vision*, pages 1905–1914, 2021. 1, 2, 3, 6
- [48] Yinhuai Wang, Jiwen Yu, and Jian Zhang. Zero-shot image restoration using denoising diffusion null-space model. *arXiv preprint arXiv:2212.00490*, 2022. 1

- [49] Yufei Wang, Wenhan Yang, Xinyuan Chen, Yaohui Wang, Lanqing Guo, Lap-Pui Chau, Ziwei Liu, Yu Qiao, Alex C Kot, and Bihan Wen. Sinsr: diffusion-based image super-resolution in a single step. In *Proceedings of the IEEE/CVF Conference on Computer Vision and Pattern Recognition*, pages 25796–25805, 2024. 2, 6
- [50] Zhou Wang, Alan C Bovik, Hamid R Sheikh, and Eero P Simoncelli. Image quality assessment: from error visibility to structural similarity. *IEEE transactions on image processing*, 13(4):600–612, 2004. 6
- [51] Zhengyi Wang, Cheng Lu, Yikai Wang, Fan Bao, Chongxuan Li, Hang Su, and Jun Zhu. Prolificdreamer: High-fidelity and diverse text-to-3d generation with variational score distillation. *Advances in Neural Information Processing Systems*, 36, 2024. 2, 3
- [52] Pengxu Wei, Ziwei Xie, Hannan Lu, Zongyuan Zhan, Qixiang Ye, Wangmeng Zuo, and Liang Lin. Component divide-and-conquer for real-world image super-resolution. In *Computer Vision—ECCV 2020: 16th European Conference, Glasgow, UK, August 23–28, 2020, Proceedings, Part VIII 16*, pages 101–117. Springer, 2020. 6, 9
- [53] Rongyuan Wu, Lingchen Sun, Zhiyuan Ma, and Lei Zhang. One-step effective diffusion network for real-world image super-resolution. *arXiv preprint arXiv:2406.08177*, 2024. 2, 3, 4, 6, 9
- [54] Rongyuan Wu, Tao Yang, Lingchen Sun, Zhengqiang Zhang, Shuai Li, and Lei Zhang. Seesr: Towards semantics-aware real-world image super-resolution. In *Proceedings of the IEEE/CVF conference on computer vision and pattern recognition*, pages 25456–25467, 2024. 1, 2, 6
- [55] Rui Xie, Ying Tai, Kai Zhang, Zhenyu Zhang, Jun Zhou, and Jian Yang. Addsr: Accelerating diffusion-based blind super-resolution with adversarial diffusion distillation. *arXiv preprint arXiv:2404.01717*, 2024. 2, 6, 9, 11
- [56] Sidi Yang, Tianhe Wu, Shuwei Shi, Shanshan Lao, Yuan Gong, Mingdeng Cao, Jiahao Wang, and Yujiu Yang. Maniqa: Multi-dimension attention network for no-reference image quality assessment. In *Proceedings of the IEEE/CVF Conference on Computer Vision and Pattern Recognition*, pages 1191–1200, 2022. 6
- [57] Tao Yang, Rongyuan Wu, Peiran Ren, Xuansong Xie, and Lei Zhang. Pixel-aware stable diffusion for realistic image super-resolution and personalized stylization. *arXiv preprint arXiv:2308.14469*, 2023. 1, 2, 6
- [58] Junho Yim, Donggyu Joo, Jihoon Bae, and Junmo Kim. A gift from knowledge distillation: Fast optimization, network minimization and transfer learning. In *Proceedings of the IEEE conference on computer vision and pattern recognition*, pages 4133–4141, 2017. 2
- [59] Tianwei Yin, Michaël Gharbi, Taesung Park, Richard Zhang, Eli Shechtman, Fredo Durand, and William T Freeman. Improved distribution matching distillation for fast image synthesis. *arXiv preprint arXiv:2405.14867*, 2024. 2
- [60] Tianwei Yin, Michaël Gharbi, Richard Zhang, Eli Shechtman, Fredo Durand, William T Freeman, and Taesung Park. One-step diffusion with distribution matching distillation. In *Proceedings of the IEEE/CVF Conference on Computer Vision and Pattern Recognition*, pages 6613–6623, 2024. 2
- [61] Fanghua Yu, Jinjin Gu, Zheyuan Li, Jinfan Hu, Xiangtao Kong, Xintao Wang, Jingwen He, Yu Qiao, and Chao Dong. Scaling up to excellence: Practicing model scaling for photo-realistic image restoration in the wild. In *Proceedings of the IEEE/CVF Conference on Computer Vision and Pattern Recognition*, pages 25669–25680, 2024. 1, 2, 6, 11
- [62] Zongsheng Yue, Jianyi Wang, and Chen Change Loy. Resshift: Efficient diffusion model for image super-resolution by residual shifting. *Advances in Neural Information Processing Systems*, 36, 2024. 2, 6
- [63] Kai Zhang, Jingyun Liang, Luc Van Gool, and Radu Timofte. Designing a practical degradation model for deep blind image super-resolution. In *Proceedings of the IEEE/CVF International Conference on Computer Vision*, pages 4791–4800, 2021. 1, 2, 3, 6
- [64] Lin Zhang, Lei Zhang, and Alan C Bovik. A feature-enriched completely blind image quality evaluator. *IEEE Transactions on Image Processing*, 24(8):2579–2591, 2015. 6, 9
- [65] Lvmin Zhang, Anyi Rao, and Maneesh Agrawala. Adding conditional control to text-to-image diffusion models. In *Proceedings of the IEEE/CVF International Conference on Computer Vision*, pages 3836–3847, 2023. 2
- [66] Richard Zhang, Phillip Isola, Alexei A Efros, Eli Shechtman, and Oliver Wang. The unreasonable effectiveness of deep features as a perceptual metric. In *Proceedings of the IEEE conference on computer vision and pattern recognition*, pages 586–595, 2018. 2, 3, 6
- [67] Xindong Zhang, Hui Zeng, Shi Guo, and Lei Zhang. Efficient long-range attention network for image super-resolution. In *European conference on computer vision*, pages 649–667. Springer, 2022. 1
- [68] Yuehan Zhang, Bo Ji, Jia Hao, and Angela Yao. Perception-distortion balanced admm optimization for single-image super-resolution. In *European Conference on Computer Vision*, pages 108–125. Springer, 2022. 6